

Structural principles to steer the selectivity of the electrocatalytic reduction of aliphatic ketones on platinum

Christoph J. Bondue¹, Federico Calle-Vallejo², Marta C. Figueiredo¹ and Marc T. M. Koper^{1*}

Due to a general feedstock shift, the chemical industry is charged with the task of finding ways to transform renewable ketones into value-added products. A viable route to do so is the electrochemical hydrogenation of the carbonyl functional group. Here we report a study on acetone reduction at platinum single-crystal electrodes using online electrochemical mass spectroscopy, in situ Fourier transform infrared spectroscopy and density functional theory calculations. Acetone reduction at platinum displays a remarkable structural sensitivity: not only the activity, but also the product distribution depends on the surface crystallographic orientation. At Pt(111) neither adsorption nor hydrogenation occur. A decomposition reaction that deactivates the electrode happens at Pt(100). Acetone reduction proceeds at the (110) steps: Pt[(n - 1)(111) × (110)] electrodes produce 2-propanol and Pt[(n + 1)(100) × (110)] electrodes produce propane. Using density functional theory calculations, we built a selectivity map to explain the intricacies of the acetone reduction on platinum. Finally, we extend our conclusions to the reduction of higher aliphatic ketones.

The pyrolysis of lignin-rich waste materials and biomass to bio-oils has the potential to become a new, valuable source of aromatic platform chemicals¹. However, bio-oils consist of carboxylic acids, ketones and aldehydes that need further refinement²⁻⁴. Therefore, studies on the electrochemical hydrogenation of carbonyl compounds, such as acetophenone⁵, benzaldehyde^{6,7}, 5-hydroxymethylfurfural⁸⁻¹⁰ or ethyl pyruvate^{11,12} have received renewed attention, as they might give valuable insight into the electrorefinement of biomass. The electrochemistry of the ethyl pyruvate is also interesting because it is the standard substrate of the Orto reaction by which α -keto esters can be enantioselectively hydrogenated using heterogeneous catalysis¹³. However, each of these carbonyl compounds features a second functional group that is also susceptible to hydrogenation. For instance, the phenyl ring of acetophenone behaves similarly to that of benzene, which has a rich and rather complex electrochemistry of its own¹⁴.

To provide fundamental knowledge on the electrochemistry of carbonyl functional groups, here we study the electrochemical reduction of acetone as a model system for the electroreduction of carbonyl compounds. As acetone is the simplest ketone, its reduction is not convoluted by the presence of additional functional groups or by the formation of acetals. It was shown previously that acetone can be reduced electrochemically at polycrystalline platinum electrodes¹⁵⁻¹⁹ to give both propane and 2-propanol^{16,17}. Hazzazi et al. showed that ethyl pyruvate adsorbs preferentially at the (110) steps on Pt electrodes and, via CO formation, at the Pt(100) terraces¹¹. This suggests a strong influence of the surface structure on the electrochemistry of ketones.

In this study, we employed single-crystal platinum electrochemistry in combination with in situ and online techniques (Fourier transform infrared spectroscopy (FTIR) and online electrochemical mass spectroscopy (OLEMS)) to show that the activity, selectivity and extent of the catalytic poisoning of acetone electroreduction are highly sensitive to the platinum surface structure. Using density

functional theory (DFT) calculations, we propose detailed pathways for the electrocatalytic reduction of acetone to give 2-propanol and propane, and show that the product selectivity is driven by the coordination of the active sites.

Results

Acetone reduction at single-crystal platinum electrodes. Figure 1a shows the cyclic voltammograms (CVs) at stepped Pt(111)-type single-crystal electrodes in an electrolyte of 0.1 M H₂SO₄ that contained 0.1 M acetone. At all the stepped electrodes a peak due to hydrogen desorption from the (110) step sites is observed in the positive-going sweep at approximately 0.12 V. In the blank electrolyte the corresponding reduction peak appears in the negative-going scan at the same potential. Such a peak is missing in the presence of acetone (Supplementary Figs. 1–6) and indicates the strong adsorption of acetone at the (110) step sites (the interaction between the (110)-step sites and acetone is rather strong, as explained further in Supplementary Fig. 7 and Supplementary Note 2). Hydrogen adsorption is only possible once the acetone is fully removed from the surface. No acetone adsorption is observed at the Pt(111) terraces as the presence of acetone does not suppress the sulfate spike or the hydrogen underpotential deposition peak at Pt(111) (Supplementary Fig. 1 and Supplementary Note 1).

In the presence of acetone, a peak at 0.05 V appears in the negative-going sweep at Pt(554), Pt(553), Pt(331) and Pt(110), which indicates the reduction of the ketone. At an electrode with long terraces, such as Pt(15,15,14), only a faint shoulder is observed, and any indication for acetone reduction is missing at Pt(111). Given that acetone does not adsorb on (111) terraces, the inactivity of Pt(111) is not surprising. Figure 1b illustrates that the activity for acetone reduction only stems from the (110) step sites: the current density at 0.05 V increases linearly as the theoretical step density increases from 0 (that is, Pt(111)) to 0.23 (that is, Pt(553)). However, for step densities larger than 0.23 the current density plateaus (the same behaviour is

¹Leiden Institute of Chemistry, Leiden University, Leiden, The Netherlands. ²Departament de Ciència de Materials i Química Física, Institut de Química Teòrica i Computacional (IQTCUB), Universitat de Barcelona, Barcelona, Spain. *e-mail: m.koper@chem.leidenuniv.nl

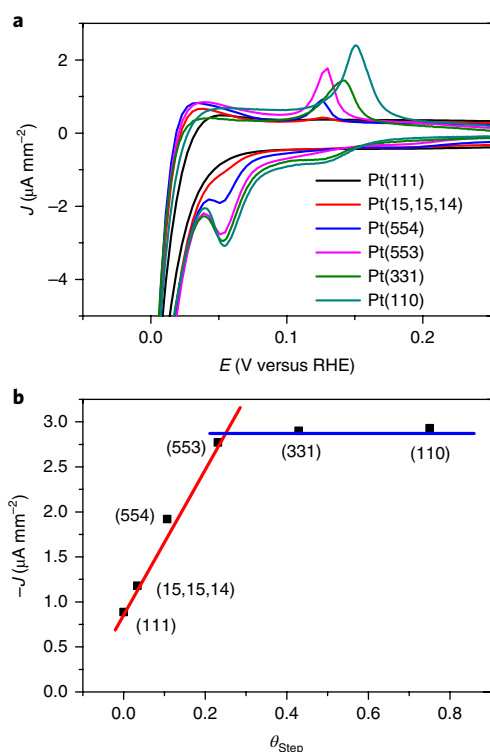


Fig. 1 | Influence of the step density of Pt[(*n* - 1)(111) × (110)] electrodes on acetone reduction. **a** CVs at various stepped Pt(111) electrodes (Pt[(*n* - 1)(111) × (110)]) in 0.1 M H₂SO₄ that contained 0.1 M acetone. **b** Current density at 0.05 V plotted as a function of the theoretical step density (no (1 × 2) reconstruction is considered). Full potential sweeps for each electrode both in the blank electrolyte and in acetone-containing electrolyte are given in Supplementary Figs. 1–6. A plot of the current density versus the charge of the hydrogen desorption peak (as a measure for the real step density) is given in Supplementary Fig. 8.

observed in Supplementary Fig. 8 in which the current density is plotted versus the experimentally determined surface step density, as determined in Supplementary Note 3). In principle, this means that the activity of the individual (110) steps decreases for high densities. In other words, the nominal turnover frequency per step site is lower at Pt(110) compared to that at Pt(553).

As long as the number of adsorption sites is the only limiting factor, the current density follows the step density linearly. However, steric hindrance or any other step–step interaction between adsorbed species may limit the maximal achievable surface concentration. This situation appears to be achieved at Pt(553). Increasing the step density further does not result in a higher surface concentration. As is shown later, individual step sites on Pt(110) are predicted to be more active than those on Pt(553) because their generalized coordination number (CN) (ref. ²⁰ and Supplementary Table 2) is close to optimal, but experiments suggest that they participate less frequently in acetone hydrogenation. There appears to be a compensation effect between the density of active sites and their intrinsic activity. A similar effect was invoked for the hydrogenation of benzene at stepped Pt(111) terraces²¹ and for oxygen reduction on stepped Pt(111) (ref. ²²).

Hydrogen evolution and acetone reduction are the only reactions to occur at stepped Pt(*n*(111) × (110)) electrodes. That is, there is no side reaction that leads to the poisoning of the electrode. As discussed in Supplementary Note 4, this is derived from Supplementary Fig. 9a in which a Pt(553) electrode has been cycled for a prolonged period of time without any effect on the shape of

the CV. This is in contrast to other aldehydes (for example, acetaldehyde) that interact with platinum surfaces by cleavage of the C–C bond, which results in the accumulation of CH_x species and carbon monoxide on the electrode²³.

We then analysed the effect of changing the terrace symmetry from (111) to (100) while keeping the same type of steps. Figure 2a shows the CVs obtained in an electrolyte of 0.1 M H₂SO₄ that contained 0.1 M acetone at stepped Pt(100) electrodes. A shoulder prior to hydrogen evolution appears in the CV of Pt(10,1,0) and, more prominently, of Pt(510) in the presence of acetone. The shoulder indicates ketone reduction, and is missing in the CV of pristine Pt(100). Similar to the stepped Pt(111) electrodes, the activity of stepped Pt(100) electrodes increases with step density. The most likely interpretation for this observation is that the electrochemical hydrogenation takes place at the (110) step sites. Computational studies suggest that the activity for acetone reduction at stepped Pt(100) electrodes stems from the step sites (see below), whereas the terraces are inactive for acetone reduction. In addition, the discussion of Supplementary Figs. 10–12 in Supplementary Note 5 provides further arguments as to why the CV data also suggest that the active surface sites for acetone reduction are the step sites.

Aside from acetone reduction, a reaction occurs at stepped Pt(100) electrodes that leads ultimately to poisoning: Supplementary Fig. 9b shows that Pt(510) loses all its activity for acetone reduction after the third cycle. To identify the active surface site for the poisoning reaction, we conducted the potential opening experiment shown in Fig. 2b. Each cycle in Fig. 2b is the first potential scan recorded at a freshly prepared Pt(100) electrode in an electrolyte of 0.1 M H₂SO₄ that contained 0.1 M acetone. As long as the lower potential window remained above 0.7 V, only capacitive currents are observed in the CV. However, when the lower potential limit goes below 0.7 V an oxidation current appears in the negative-going scan, with a corresponding oxidation current in the potential region between 0.7 and 0.85 V in the subsequent positive-going scan. These results suggest that acetone is oxidized at the (100) terraces at potentials below 0.7 V. This oxidation is incomplete, because further oxidation takes place in the potential region between 0.7 and 0.85 V.

When we accumulate products of incomplete acetone oxidation by exposing a Pt(510) electrode for 2 minutes to an acetone-containing electrolyte at 0.45 V, the electrode loses its ability to reduce acetone (Supplementary Fig. 13 and Supplementary Note 6). However, exposing the electrode for 2 minutes to the same solution at 0.85 V, where acetone does not undergo a reaction, does not impair the acetone reduction in the subsequent negative-going sweep. This suggests that the oxidation process observed at Pt(100) in the potential range between 0.7 and 0.45 V causes the poisoning of the stepped Pt(100) electrode. That is, the Pt(100) terraces are the active surfaces sites for electrode poisoning. Although we do not study the nature of the poisoning reaction in detail, it is interesting to note its sensitivity to the crystallographic orientation of the electrode.

Product distribution of acetone reduction. To demonstrate the influence of surface orientation on the product distribution, in Fig. 3 we show the OLEMS results obtained at Pt(553) and Pt(510) during potential steps into the potential window of acetone reduction. After each step, an intense signal in the ionic current for mass 2 is observed (Fig. 3b,e), which corresponds to hydrogen evolution. As the signal intensity at both crystals is roughly the same, we can infer that the sensitivity for the two experimental set-ups is comparable. Parallel to the hydrogen evolution, signals in the ionic currents for masses 27, 29 and 44 with an intensity ratio for $I_{29}:I_{27}:I_{44}$ of 100:43:24 are observed in the experiments conducted at Pt(510) (Fig. 3c). Only faint signals for the same masses are observed for Pt(553) (Fig. 3f).

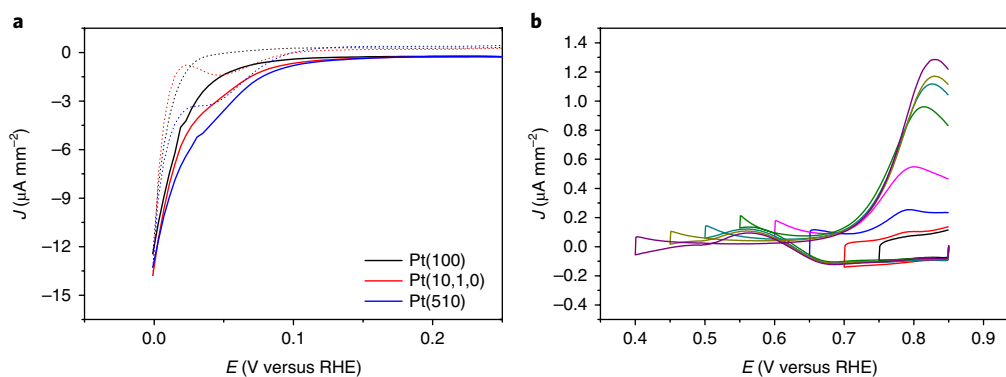


Fig. 2 | Cyclic voltammetry of acetone reduction at Pt[($n+1$)(100) \times (110)] electrodes. **a, CVs at stepped Pt(100) electrodes (Pt[($n+1$)(100) \times (110)]) in 0.1M H₂SO₄ that contains 0.1M acetone. Solid lines, negative-going sweep; dotted lines, positive-going sweep. **b**, Potential opening experiment at a Pt(100) electrode. Full potential sweeps for each electrode are given in Supplementary Figs. 10–12. Sweep rate, 0.05 V s⁻¹; potential limits, 0–0.85 V.**

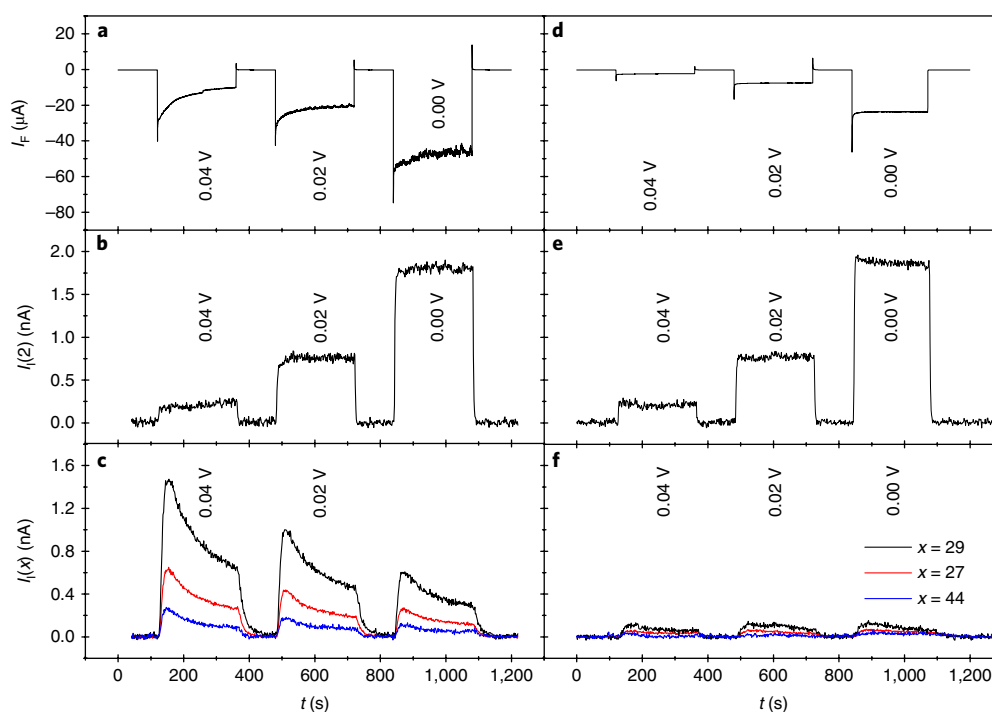


Fig. 3 | Structure sensitivity of propane formation during acetone reduction. The OLEMS results obtained at Pt(510) (left) and Pt(553) (right). The step potential program was 0.85, 0.04, 0.85, 0.02, 0.85, 0 and 0.85 V. **a,d**, Faradaic current. **b,e**, Ionic current for mass 2. **c,f**, Ionic current for masses 29 (black), 27 (red) and 44 (blue). The electrolyte was 0.1M H₂SO₄ that contained 0.1 M acetone.

The observed masses and intensity ratios correspond to the fragmentation pattern of propane, and indicates a significant acetone reduction to propane on Pt(510). As only a faint signal for propane formation was observed during acetone reduction at Pt(553), we deduced that the hydrocarbon is only a minor product of acetone reduction. Hence, the dominant product of acetone reduction at Pt(553) electrodes should be 2-propanol. Note that alcohols are difficult to detect by OLEMS because they do not pass readily from the aqueous phase into the vacuum of the mass spectrometer.

The FTIR spectra in Fig. 4 confirm the assertion that acetone is reduced to 2-propanol at Pt[($n-1$)(111) \times (110)] electrodes. After a potential step to 0.05 V at Pt(110), two bands at 2,971 cm⁻¹ and 2,877 cm⁻¹ appear. These bands correspond to the asymmetric and symmetric stretching vibrations of the methyl groups of 2-propanol at $\nu(\text{CH}_3)_{\text{as}}=2,971$ cm⁻¹ and at $\nu(\text{CH}_3)_{\text{s}}=2,888$ cm⁻¹ (ref. 24).

On the other hand, propane has only a single band at 2,940 cm⁻¹ due to both $\nu(\text{CH}_3)_{\text{as}}$ and $\nu(\text{CH}_3)_{\text{s}}$ (ref. 25). The appearance of two bands, therefore, strongly indicates that acetone is reduced only to 2-propanol at Pt(110). If propane was formed, a third band would be expected in Fig. 4. Although perfect selectivity cannot be proven with the employed techniques, it can be asserted that acetone is reduced to 2-propanol with good selectivity at Pt[($n-1$)(111) \times (110)] electrodes.

Aside from the positive bands at 2,971 cm⁻¹ and 2,877 cm⁻¹, there are three negative bands at 1,697 cm⁻¹, 1,370 cm⁻¹ and 1,237 cm⁻¹ in Fig. 4. These bands correspond to the symmetric stretching vibration of the C–O bond ($\nu(\text{C–O})_{\text{s}}=1,710$ cm⁻¹), the symmetric deformation vibration of the methyl groups ($\delta(\text{Me})_{\text{as}}=1,361$ cm⁻¹) and the asymmetric stretching vibration of the carbon skeleton ($\nu(\text{Me–C–Me})_{\text{as}}=1,220$ cm⁻¹) of free acetone^{26,27}. These bands

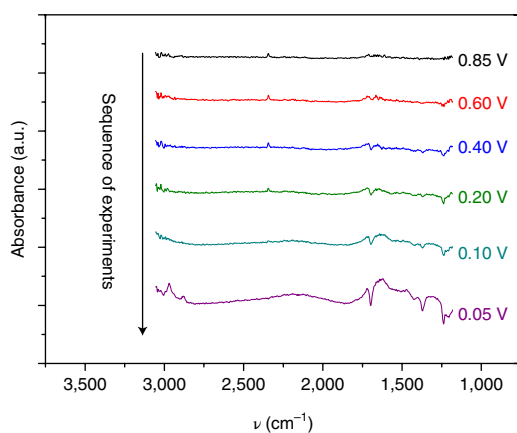


Fig. 4 | FTIR spectra obtained at Pt(110) and at the indicated potentials in an electrolyte of 0.1 M H₂SO₄ that contained 0.1 M acetone.

suggest the depletion of acetone from the thin layer between the electrode and the prism. This already happens at potentials more positive than 0.05 V and before the formation of 2-propanol, which indicates the electrochemical consumption of acetone. Given our conclusion that acetone starts to adsorb at Pt(553) in the potential range between 0.4 and 0.6 V (Supplementary Fig. 7), it is likely that the negative bands are due to the adsorption of acetone.

The FTIR spectra in Fig. 4 do not feature any positive bands that could be assigned to adsorbed acetone. However, the large background due to water and acetone in the gap between the prism and the electrode makes it difficult to observe weak bands in FTIR spectra. In the Supplementary Information, we provide Raman spectra that show that acetone adsorbed in a Raman active mode experiences a weakening of the C–O binding strength (Supplementary Fig. 14 in Supplementary Note 7).

Computational modelling of acetone reduction. To gain insight into the intriguing structure-sensitive selectivity of acetone reduction, we used DFT calculations. We modelled acetone reduction on six sites at Pt surfaces (the structures and active sites are given in Supplementary Fig. 16 and Supplementary Note 8) through the reaction networks shown in Supplementary Fig. 15. After modelling all the possible pathways (Supplementary Fig. 15), including those starting with propenol, the enol tautomer of acetone, we concluded that the most favourable pathways for acetone reduction to 2-propanol and propane, namely, those with the lowest overpotential, are those in Fig. 5. Both pathways proceed via acetone molecular adsorption and subsequent hydrogenation to $^*\text{CH}_3\text{COHCH}_3$. If the carbon atom bound to the surface of this intermediate is hydrogenated, 2-propanol is formed. Conversely, if the C–O bond is cleaved, propane and water are produced. Thus, there are two key factors for acetone reduction: first, whether acetone adsorbs or not determines the activity of the catalyst; second, the relative ease of protonation or C–O bond scission of $^*\text{CH}_3\text{COHCH}_3$ determines the selectivity of the reaction.

First, we focus on the activity trends among Pt sites. In Fig. 6, we provide separate coordination-activity plots for 2-propanol and propane production modelled following the pathways in Fig. 5. For 2-propanol production, the most active surface is Pt(110). As only two electrons are transferred in this reaction, the top of the volcano and the equilibrium potential coincide in Fig. 6a²⁸. The orange line in the plot (weak binding sites) corresponds to acetone hydrogenation to $^*\text{CH}_3\text{COHCH}_3$ being the potential-determining step. The green line (strong binding sites) corresponds to the hydrogenation of $^*\text{CH}_3\text{COHCH}_3$ to produce 2-propanol

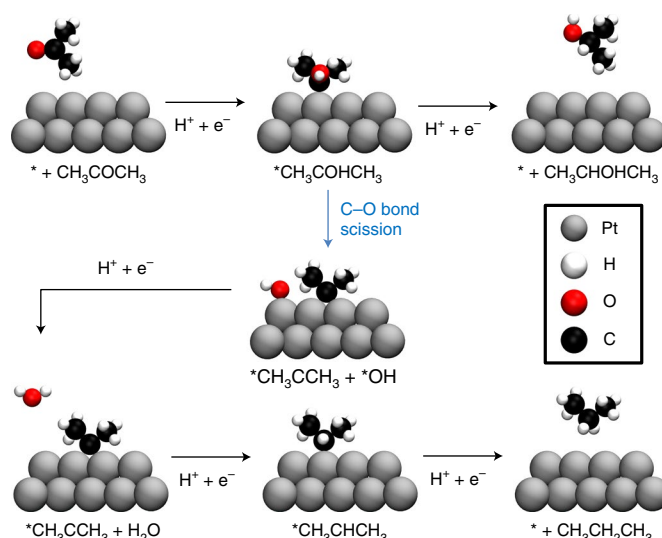


Fig. 5 | The most favourable reaction pathways computed for acetone reduction to 2-propanol and propane at Pt electrodes. The entire reaction networks from which they were derived are given in Supplementary Fig. 15.

being the potential-determining step. The inset shows the correlation between $\overline{\text{CN}}$ and the adsorption energies of acetone. The red dashed line at $\overline{\text{CN}} \approx 6.0$ corresponds to the limit of exothermic acetone adsorption on Pt facets (Supplementary Fig. 18b in Supplementary Note 8 shows that for $\overline{\text{CN}} \leq 5.8$, acetone adsorption energies are more favourable than those of $^*\text{H}$).

Figure 6b shows that Pt(510) is predicted to be the most active surface under study for propane production. The orange line (weak binding) in the plot corresponds, again, to acetone hydrogenation. The blue line (strong binding) represents the hydrogenation of $^*\text{CH}_3\text{CCH}_3$ to $^*\text{CH}_3\text{CHCH}_3$. The inset shows that for $\overline{\text{CN}} < 6.2$ (purple line in the main panel), $^*\text{CH}_3\text{COHCH}_3 + ^* \rightarrow ^*\text{CH}_3\text{CCH}_3 + ^*\text{OH}$ is thermodynamically favourable, which is necessary to shift the selectivity toward propane production.

Furthermore, Fig. 5 shows that the pathway of acetone reduction bifurcates before 2-propanol is formed. This suggests that once the alcohol is formed, no further reduction is possible. Indeed, we arrived at the same conclusions experimentally: Supplementary Fig. 19 and the related discussion in Supplementary Note 9 show that 2-propanol cannot be reduced at the Pt(510) electrode under the same conditions as acetone is reduced to propane.

It is useful to determine whether and how coordination influences the pathway bifurcation. In Fig. 7 we overlap Fig. 6a,b together with the H₂ evolution trends from Pohl et al.²⁹ to provide a selectivity map that predicts the most favourable product of acetone reduction and its onset potential based on the geometry of the Pt active sites. Essentially, we detect three regions:

(1) For a large coordination number ($\overline{\text{CN}} > 6.6$, red lines in Fig. 7), $^*\text{H}$ adsorption and H₂ evolution are the most favourable (Supplementary Fig. 18b), so the sites are inactive for acetone reduction. This is the case for the terrace sites at Pt(111) and Pt(100).

(2) For an intermediate coordination number, the orange line in Fig. 7 ($6.0 < \overline{\text{CN}} < 6.6$) marks the region in which 2-propanol formation is more favourable than H₂ evolution, but acetone molecular adsorption is endothermic. On sites with a coordination number in the range $5.5 < \overline{\text{CN}} < 6.0$ (green line in Fig. 7), acetone adsorption becomes exothermic and more favourable than that of $^*\text{H}$ (Supplementary Fig. 18b), and $^*\text{CH}_3\text{COHCH}_3$ hydrogenation is more favourable than the scission of the C–O bond, so that 2-propanol predominates in the product distribution. This is the case for Pt(110) and for the step sites in Pt(553).

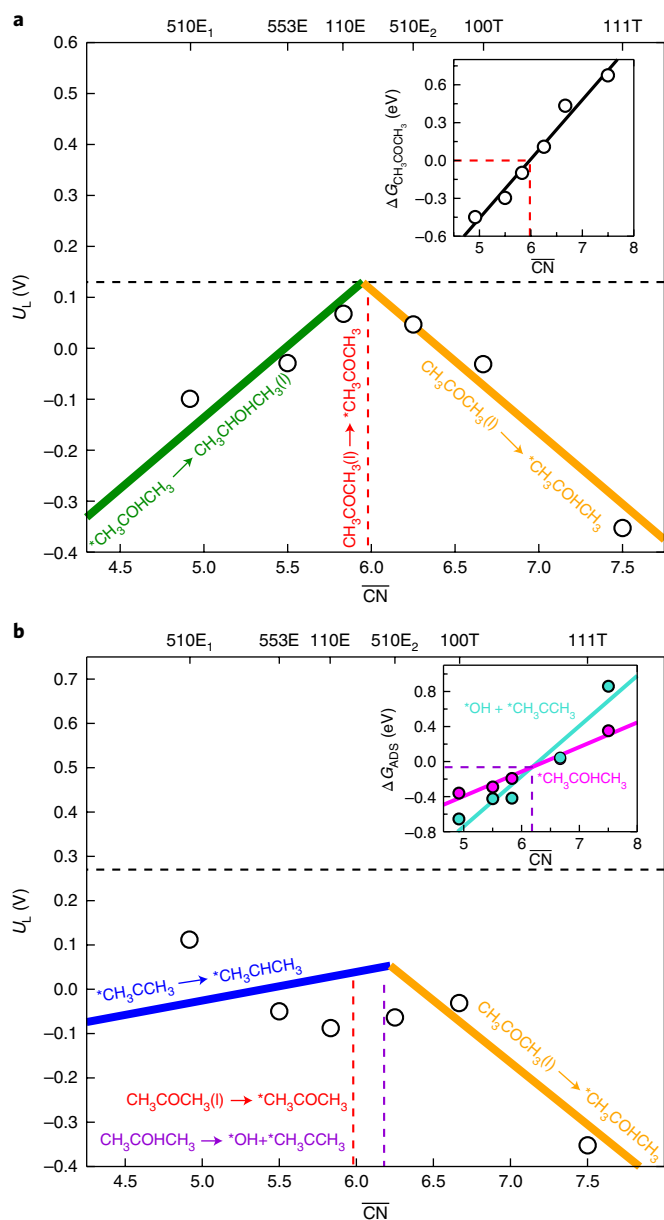


Fig. 6 | Coordination-activity plots for acetone reduction. a, b, Reduction to 2-propanol (**a**) and propane (**b**). Six different Pt surface sites were studied (top x axis and Supplementary Fig. 16). The most favourable onset potentials (U_L) are reported for each site. The dots are calculated data points from the DFT simulations. The orange, green and blue lines are from Supplementary Fig. 18a and result from correlations between generalized coordination numbers and adsorption energies. The mean absolute errors between the fits and the calculated data points are, in all cases, smaller than 0.10 eV. The black dashed lines correspond to the equilibrium potentials. The red line comes from the inset in **a** and separates sites with/without (left/right) exothermic acetone adsorption. The purple line from the inset in **b** and separates sites for which $^*CH_3COHCH_3 + ^* \rightarrow ^*CH_3CCH_3 + ^*OH$ is exothermic/endergonic (left/right). 510E₁ and 510E₂, step-edge site on Pt(510) as defined in Supplementary Figure 16; 100T, (100) terrace site; 111T, (111) terrace site.

(3) For a low coordination number ($\overline{CN} < 5.5$, blue line in Fig. 7), the cleavage of the C–O bond in *CH_3COHCH_3 is rather favourable, such that propane is the preferred product. This is the case for the undercoordinated step sites on Pt(510) (510E₁ sites in Fig. 7).

The slopes of the lines in Fig. 7 come from Fig. 6 and give an account of the structural dependence of the potential-determining steps of each reaction pathway. The orange and green lines are steeper than the blue one because in the former two the reaction energy involves only a single adsorbed intermediate. Conversely, the blue line involves two adsorbed species (one as a reactant, the other as a product), which leads to a small slope because of the similarity between the adsorbed species. This is illustrated in Supplementary Fig. 18, in which it is also shown that the mean absolute errors between the calculated data points and the fits are below 0.10 eV in all cases. The red lines for H₂ evolution have a small slope because the variations in hydrogen adsorption energy as a function of the coordination of the active sites are typically small (although systematic)²⁹.

Extension of the results to other aliphatic ketones. The results obtained for the electrocatalytic hydrogenation of acetone at platinum single crystals were extended to butanone and 3-pentanone. In Supplementary Note 10, Supplementary Figs. 20–28 compare the CVs in an acetone-containing electrolyte with those recorded in butanone- and pentanone-containing electrolytes. Essentially, the same trends as for acetone are observed—with the increasing step density of the Pt(111)-type electrodes, the activity increases (Supplementary Fig. 29). However, as the carbon chain becomes longer, ketone reduction is shifted to more negative potentials. Although acetone reduction takes place in a well-defined peak, butanone reduction takes place in a shoulder and 3-pentanone reduction is barely distinguishable from hydrogen evolution. This might reflect a better stabilization of the C–O bond by hyperconjugation with the σ orbital of a C–C bond in butanone and 3-pentanone compared to hyperconjugation with the σ -orbital of a C–H bond in acetone.

A further difference between acetone, butanone and 3-pentanone becomes evident from Supplementary Fig. 20. From the reversibility of the sulfate spike at Pt(111) we inferred that acetone does not adsorb at this electrode. Although the spike in the first negative-going scan appears in the presence of butanone and 3-pentanone, it is lost in the subsequent positive-going scan. In the presence of 3-pentanone, the spike is shifted to more positive potentials and hydrogen adsorption is shifted to more negative potentials, both in the presence of butanone and of pentanone. The altered adsorption energy for hydrogen and the change in the peak potential for sulfate adsorption indicate the adsorption of butanone and 3-pentanone, respectively. As the hydrogen underpotential deposition is not severely suppressed, the adsorption of butanone and 3-pentanone is weak and might be the result of enhanced van der Waals interactions due to the longer carbon chains.

From the CVs in Supplementary Figs. 26–28 and 30 it is less obvious that the reduction of butanone and 3-pentanone takes place at the steps of the Pt(100)-type electrodes. However, this is evident from the OLEMS results displayed in Supplementary Fig. 31 and discussed in Supplementary Note 11. As in Fig. 3, steps from 0.85 V into the potential region of butanone reduction were conducted and, in parallel, the mass spectrometric response was measured. The ionic current measured for mass 43 indicates the formation of butane, which is most prominent at Pt(510). Comparatively small amounts of butane are formed at pristine Pt(100). Hence, the reduction of higher aliphatic ketones proceeds at the steps of Pt(100)-type surfaces as well. In addition, no formation of butane was observed at Pt(553). Therefore, it can be concluded that the higher ketones are also reduced to the corresponding alcohol at stepped Pt(111)-type electrodes.

Discussion

Figures 1 and 2 show that acetone reduction does not proceed at the (111) and (100) basal planes of platinum. The activity of the

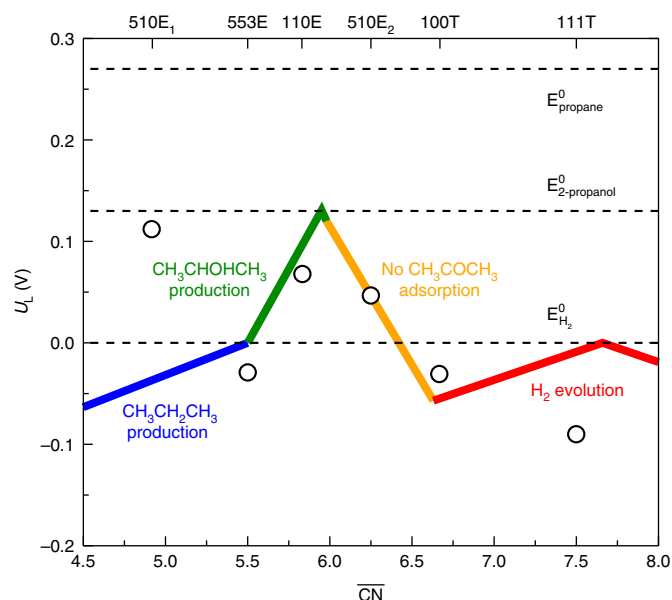


Fig. 7 | Structure-sensitive selectivity map for acetone reduction to 2-propanol and propane. The top x axis locates the six different Pt sites under study (Supplementary Fig. 16). The most favourable onset potentials (U_i) are reported in each case. The most active sites are the steps on Pt(110) for 2-propanol production, and the (110) steps at Pt(510) for propane production. Black dashed lines represent the equilibrium potentials. Open circles are calculated data points from the DFT simulations. The data for H_2 evolution (red line) come from Pohl et al.²⁹, the orange, green and blue lines come from Fig. 6 and are linear regressions built from six data points in each case. Further details are given in Supplementary Note 8 and Supplementary Fig. 18.

platinum electrodes, thus, depends on the presence of steps. The DFT calculations (Figs. 6 and 7) show that the interaction of acetone with Pt(111) and Pt(100) is energetically unfavourable due to the high coordination number of their surface atoms. Based on our experimental results, it was difficult to assess whether acetone reduction at stepped Pt(100) electrodes proceeds at (100) terraces and/or at step sites. Figure 7 shows that the inactivity for acetone reduction is inherent to the (100) terraces and not caused by the poisoning reaction that occurs at it. Hence, acetone reduction takes place at the step sites of both Pt[($n-1$)(111)×(110)] and Pt[($n+1$)(100)×(110)] electrodes. However, experiments suggest that the poisoning of the electrode occurs due to a reaction that takes place at (100) terraces. This poisoning reaction was not subjected to detailed investigation in this work as our emphasis was on the selectivity of the hydrogenation reaction, but it is observed that this reaction leads to the accumulation of incomplete oxidation products at Pt(100)-type electrodes, which ultimately results in the full deactivation of the catalyst (Supplementary Fig. 9b). Furthermore, the poison can be removed oxidatively.

OLEMS (Fig. 3) and FTIR (Fig. 4) results show that the nature of the steps has a significant influence on product distribution. Acetone is reduced predominantly to 2-propanol at the steps of Pt[($n-1$)(111)×(110)], whereas propane is formed at the step sites of Pt[($n+1$)(100)×(110)]. The selectivity map in Fig. 7 explains that the different products are due to the dissimilar stabilization of reaction intermediates, which is a function of the coordination number of the active sites. The selectivity-determining intermediate is *CH_3COHCH_3 and the competing reactions are its hydrogenation and the cleavage of its C–O bond. Note that once 2-propanol is desorbed from the surface, it neither adsorbs again nor undergoes further reduction according to both experiments and calculations.

In other words, 2-propanol is not an intermediate of propane evolution from acetone, according to our observations.

In a previous paper, we suggested that the *CH_3COHCH_3 intermediate does not form from the keto tautomer³⁰. Instead, acetone adsorbs either as propenol (its enol tautomer) or as protonated acetone from the solution. We have assessed the effect of propenol as a prime reactant on our conclusions for Pt(510) and Pt(553) and the results are shown in Supplementary Fig. 17. The onset potentials are nearly the same and so are the most favourable reaction pathways, which bifurcate on *CH_3COHCH_3 and differ only in the reactant. This gives confidence in the robustness of the computational results and substantiates the findings in Figs. 5–7.

In conclusion, we investigated the electrochemical hydrogenation of aliphatic ketones at platinum single-crystal electrodes, with the emphasis on acetone. The selectivity of the reaction displays a remarkable structural sensitivity—no reaction proceeds at Pt(111) terraces, but a reaction that ultimately leads to the electrode poisoning proceeds at Pt(100). In contrast, the actual hydrogenation on stepped surfaces happens at the (110) steps to yield different products: aliphatic ketones are reduced to the corresponding alcohol at Pt(111)-type electrodes, but Pt(100)-type electrodes catalyse the hydrogenolysis to produce the respective hydrocarbon.

With the help of DFT calculations, we built a structure-sensitive selectivity map, which suggests that the inability of (111) and (100) terraces to molecularly bind acetone and the predominance of *H adsorption and H_2 evolution renders them inactive and corroborates the experimental observation that (110) steps are the active sites for acetone reduction. A semiquantitative rationale for estimating whether the main product of acetone reduction will be 2-propanol or propane, based on the coordination number of the surface active site, is also provided.

The combination of detailed experimental and computational work presented here therefore allows us to conclude that surfaces with a high generalized coordination number (Pt(111) and Pt(100)) do not adsorb acetone and are therefore inactive for the reduction of the ketone. 2-Propanol is formed at Pt(553) and Pt(110) electrodes that feature medium generalized coordination numbers and propane production occurs only at surfaces that feature low generalized coordination numbers, such as that of the Pt(510) electrode. Furthermore, computational modelling elucidates the mechanism of acetone reduction in which the pathways to the alcohol and the hydrocarbon separate before 2-propanol is formed. This explains the experimental finding that acetone can be reduced to both propane and 2-propanol, but that the reduction of 2-propanol to the hydrocarbon is not measurable at Pt(510) electrodes.

Methods

Chemicals and materials. The blank electrolyte was prepared from MilliQ water and H_2SO_4 (suprapure, Merck). The ketones used were acetone (HPLC grade, Sigma-Aldrich), butanone (>99%, Sigma-Aldrich) and 3-pentanone (>99%, Sigma-Aldrich). All the solutions were freed from oxygen by purging with argon (6.0, Linde). All potentials were measured versus a reversible hydrogen electrode (RHE) in contact with the blank electrolyte. A platinum wire was used as the counter electrode. Under acidic conditions, ketones are expected to undergo a condensation reaction³¹. To avoid both the accumulation of condensation products and the depletion of the ketone, the electrolyte was changed every hour. CVs were recorded on either a PGSTAT 12 potentiostat (Autolab) or an Iviumstat potentiostat (Ivium Technologies).

Single-crystal electrodes. Electrochemical experiments and OLEMS experiments were conducted with bead-type single crystals purchased from Icryst. Prior to each experiment the surface of the crystal was prepared by flame annealing following the protocol established by Clavilier et al.³². The used glassware was kept for at least 8 h in acidic permanganate solution. Prior to use, the glassware was rinsed with acidic peroxide solution and boiled several times in MilliQ water.

In this work, we used Pt(111), Pt(15,15,14), Pt((554), Pt(553), Pt(331) and Pt(110) electrodes. These surfaces are derived from the (111) basal plane by introducing (110) steps. Although the terrace size of the (111) electrode is in theory infinite, its length is reduced to 30 atoms in Pt(15,15,14), ten atoms in Pt(554), five atoms in Pt(553) and three atoms in Pt(331). In principle, there are

no (111) terraces in the (110) surface. The step density on these surfaces increases accordingly, defined as $\theta_{\text{step}} = 1/(n-2/3)$ (ref. 33), where n is the width of the terraces (in number of atoms). However, in reality a (1×2) reconstruction of Pt(110) is observed³⁴. In the ideal (1×2) reconstructed Pt(110) surface, every second row of (110)-step sites is missing, which reduces the step density by half and introduces (111) terraces two atoms long.

The other set of electrodes was Pt(100), Pt(10,1,0) and Pt(510). These electrodes are derived from the (100) basal plane. In theory, the terrace width of Pt(100) is infinite. By introducing (110) steps the terrace width of the Pt(10,1,0) electrode is reduced to ten atoms and that of the Pt(510) electrode to five atoms.

Online electrochemical mass spectrometry. Online mass spectra were recorded in the multiple-ion detection mode at the indicated potentials on a PrismaPlus mass spectrometer (Pfeiffer Vacuum). A vacuum better than 10^{-5} mbar throughout the experiment was achieved by a turbo molecular pump with a suction power of 60 l s^{-1} . A Teflon frit inserted into a KelF tip was used as an interface between the electrolyte and the vacuum of the mass spectrometer³⁵. The surface area of the Teflon frit was 0.8 mm^2 . Volatile compounds can diffuse through the frit and an attached capillary into the vacuum.

In this set-up, the intensity of the mass spectrometric response depends not only on the amount of products, but also on the exact geometry of the set-up. That is, the placement of the tip with respect to the electrode will influence the efficiency with which products are collected. Unfortunately, this geometry is difficult to reproduce between two different experiments and the sensitivity of the set-up might vary. To ensure comparability of the OLEMS data obtained in two different set-ups, one can observe the mass spectroscopic response for a product that has the same formation rate in both experiments. If, in this case, the same signal intensity is observed, the collection efficiency between both set-ups is the same for any product. As hydrogen evolution proceeds with very similar formation rates at Pt(553) and Pt(510), we used the signal on the ionic current for mass 2 to ensure that the collection efficiency and, therefore, the sensitivity in both experimental set-ups was the same.

Although our OLEMS results have a qualitative rather than quantitative character, we chose the OLEMS technique to study acetone reduction because of its high sensitivity (quantities that correspond to a single monolayer can be detected³⁶) and because of the possibility to work in the online mode during cyclic voltammetry. In theory, an offline approach would allow quantification of the results, but is unsuitable for the present case: an offline approach requires the accumulation of reduction products, which is not possible due to the rapid deactivation of the Pt(510).

In situ FTIR spectroscopy. FTIR spectra were recorded on a Vertex V80 (Bruker). The FTIR cell used was home-built and accommodated a prism made of calcium fluoride³⁷. By pressing the electrode with a diameter of 1 cm on the prism, a thin gap between the electrode and the prism was achieved. All the spectra were recorded with a resolution of 4 cm^{-1} and are the average over 200 scans. A background spectrum was recorded at 0.85 V versus RHE. Next, a potential step to the indicated values was performed and another spectrum was recorded, from which the background spectrum was subtracted.

Computational details. The DFT simulations were made with VASP³⁸ using the PBE functional³⁹ and the projector augmented-wave method⁴⁰. The top-most two layers of the slabs and the adsorbates were relaxed in all directions, whereas the bottom-most ones were fixed at the bulk equilibrium distances. We used a plane-wave cutoff of 450 eV , $k_{\text{p}}T = 0.2 \text{ eV}$ (extrapolating the total energies to 0 K), and the conjugate-gradient scheme until the maximal force was $< 0.05 \text{ eV \AA}^{-1}$. Monkhorst-Pack meshes⁴¹ of $6 \times 6 \times 1$, $6 \times 6 \times 1$, $6 \times 4 \times 1$, $4 \times 3 \times 1$ and $5 \times 3 \times 1$ for Pt(111), Pt(100), Pt(110), Pt(510) and Pt(553) ensured convergence of the adsorption energies within 0.05 eV . The distance between repeated images in the vertical direction was $> 14 \text{ \AA}$ and dipole corrections were used. Isolated molecules were calculated in boxes of $15 \text{ \AA} \times 15 \text{ \AA} \times 15 \text{ \AA}$ using $k_{\text{p}}T = 0.001 \text{ eV}$ and the Γ point.

The reaction energies were approximated as $\Delta G \approx \Delta E_{\text{DFT}} + \Delta \text{ZPE} - T\Delta S + \Delta E_{\text{solvation}}$ where ΔE_{DFT} is the DFT-calculated reaction energy, ΔZPE is the zero-point energy change and $T\Delta S$ is the entropy change at 298.15 K . ΔS includes all the contributions for free molecules and only the vibrational entropy for the adsorbates. Proton-electron pairs were modelled with the computational hydrogen electrode⁴². Solvation was modelled as an external correction depending on the chemical nature of the adsorbates^{43,44} (specific values are given in Supplementary Table 1. The generalized coordination number (CN) of a surface site i is calculated based on the conventional coordination numbers (CN) of its n_i nearest neighbours^{20,45,46}:

$$\overline{\text{CN}}_i = \sum_{j=1}^{n_i} \frac{\text{CN}_j}{\text{CN}_{\text{max}}} \quad (1)$$

where CN_{max} is the number of nearest neighbours of the site if in the bulk, that is 12 for a single atom. The sites under study are shown in Supplementary Fig. 17. The construction of the coordination-activity plots for various reactions is given in the

Supplementary Information and elsewhere^{22,47,48}, and the data for H_2 evolution are from Pohl et al.²⁹.

The coordinates of the reaction intermediates on Pt(110) and Pt(510) are given in Supplementary Data 1.

Data availability

All the data are available from the authors upon reasonable request.

Received: 28 May 2018; Accepted: 9 January 2019;

Published online: 4 March 2019

References

- Brown, T. R. & Brown, R. C. What role for the bioeconomy in an electrified transportation sector? *Biofuels, Bioprod. Bior.* **11**, 363–372 (2017).
- Imam, T. & Capareda, S. Characterization of bio-oil, syn-gas and bio-char from switchgrass pyrolysis at various temperatures. *J. Anal. Appl. Pyrol.* **93**, 170–177 (2012).
- Oasmaa, A., Elliott, D. C. & Korhonen, J. Acidity of biomass fast pyrolysis bio-oils. *Energy Fuels* **24**, 6548–6554 (2010).
- Abu Bakar, M. S. & Titiloye, J. O. Catalytic pyrolysis of rice husk for bio-oil production. *J. Anal. Appl. Pyrol.* **103**, 362–368 (2013).
- Villalba, M., del Pozo, M. & Calvo, E. J. Electrocatalytic hydrogenation of acetophenone and benzophenone using palladium electrodes. *Electrochim. Acta* **164**, 125–131 (2015).
- Cantu, D. C. et al. A combined experimental and theoretical study on the activity and selectivity of the electrocatalytic hydrogenation of aldehydes. *ACS Catal.* **8**, 7645–7658 (2018).
- Song, Y. et al. Hydrogenation of benzaldehyde via electrocatalysis and thermal catalysis on carbon-supported metals. *J. Catal.* **359**, 68–75 (2018).
- Kwon, Y., de Jong, E., Raoufoghaddam, S. & Koper, M. T. M. Electrocatalytic hydrogenation of 5-hydroxymethylfurfural in the absence and presence of glucose. *ChemSusChem* **6**, 1659–1667 (2013).
- Kwon, Y., Birdja, Y. Y., Raoufoghaddam, S. & Koper, M. T. M. Electrocatalytic hydrogenation of 5-hydroxymethylfurfural in acidic solution. *ChemSusChem* **8**, 1745–1751 (2015).
- Chadderdon, X. H. et al. Mechanisms of furfural reduction on metal electrodes: distinguishing pathways for selective hydrogenation of biderived oxygenates. *J. Am. Chem. Soc.* **139**, 14120–14128 (2017).
- Hazzazi, O. A. et al. Electrochemical studies of irreversibly adsorbed ethyl pyruvate on Pt{hkl} and epitaxial Pd/Pt{hkl} adlayers. *J. Electroanal. Chem.* **640**, 8–16 (2010).
- Rees, N. V. et al. In situ surface-enhanced Raman spectroscopic studies and electrochemical reduction of α -ketoesters and self condensation products at platinum surfaces. *J. Phys. Chem. C* **115**, 1163–1170 (2011).
- Orito, Y., Imai, S. & Niwa, S. Asymmetric hydrogenation of methyl pyruvate using Pt-C catalyst modified with cinchonidine. *Nippon Kagaku Kaishi* **1979**, 1118–1120 (1979).
- Baltruschat, H. & Ernst, S. Molecular adsorbates at single-crystal platinum-group metals and bimetallic surfaces. *ChemPhysChem* **12**, 56–69 (2011).
- Kita, H., Saito, K. & Katayama, A. Electroreduction of acetone on platinum in sulfuric acid solution and catalytic action of platinum and mercury electrodes. *J. Res. Inst. Catal.* **25**, 45–62 (1977).
- Bänsch, B., Härtung, T., Baltruschat, H. & Heitbaum, J. Reduction and oxidation of adsorbed acetone at platinum electrodes studied by DEMS. *J. Electroanal. Chem. Interfacial Electrochem.* **259**, 207–215 (1989).
- de Hemptinne, X. & Schunck, K. Electrochemical reduction of acetone. Electrocatalytic activity of platinumized platinum. *Trans. Faraday Soc.* **65**, 591–597 (1969).
- Horányi, G. On the adsorption of organic compounds on platinumized platinum electrodes. *J. Electroanal. Chem. Interfacial Electrochem.* **51**, 163–178 (1974).
- Horányi, G. Electrocatalytic reductive splitting of C–O and C–OH bonds at platinum electrodes. *Electrochim. Acta* **31**, 1095–1103 (1986).
- Calle-Vallejo, F. & Bandarenka, A. S. Enabling generalized coordination numbers to describe strain effects. *ChemSusChem* **11**, 1824–1828 (2018).
- Löffler, T., Bussar, R., Xiao, X., Ernst, S. & Baltruschat, H. The adsorption of ethene on vicinally stepped electrode surfaces and the effect of temperature. *J. Electroanal. Chem.* **629**, 1–14 (2009).
- Calle-Vallejo, F. et al. Why conclusions from platinum model surfaces do not necessarily lead to enhanced nanoparticle catalysts for the oxygen reduction reaction. *Chem. Sci.* **8**, 2283–2289 (2017).
- Iwasita, T. & Pastor, E. A DEMS and FTIR spectroscopic investigation of adsorbed ethanol on polycrystalline platinum. *Electrochim. Acta* **39**, 531–537 (1994).
- Zaki, M. I., Hasan, M. A. & Pasupulety, L. In situ FTIR spectroscopic study of 2-propanol adsorptive and catalytic interactions on metal-modified aluminas. *Langmuir* **17**, 4025–4034 (2001).

25. McMurry, H. L. & Thornton, V. The infrared spectra of propane and its symmetrical deuterium substituted analogs. *J. Chem. Phys.* **19**, 1014–1018 (1951).
26. Dellepiane, G. & Overend, J. Vibrational spectra and assignment of acetone, $\alpha\alpha$ acetone- d_3 and acetone- d_6 . *Spectrochim. Acta* **22**, 593–614 (1966).
27. Avery, N. R. EELS identification of the adsorbed species from acetone adsorption on Pt(111). *Surf. Sci.* **125**, 771–786 (1983).
28. Koper, M. T. M. Thermodynamic theory of multi-electron transfer reactions: implications for electrocatalysis. *J. Electroanal. Chem.* **660**, 254–260 (2011).
29. Pohl, M. D., Watzel, S., Calle-Vallejo, F. & Bandarenka, A. S. Nature of highly active electrocatalytic sites for the hydrogen evolution reaction at Pt electrodes in acidic media. *ACS Omega* **2**, 8141–8147 (2017).
30. Bondue, C. J. & Koper, M. T. M. A mechanistic investigation on the electrocatalytic reduction of aliphatic ketones at platinum. *J. Catal.* **369**, 302–311 (2019).
31. Nielsen, A. T. & Houlihan, W. J. The Aldol Condensation. *Organic Reactions* <https://onlinelibrary.wiley.com/doi/full/10.1002/0471264180.or016.01> (2004).
32. Clavilier, J., Armand, D., Sun, S. G. & Petit, M. Electrochemical adsorption behaviour of platinum stepped surfaces in sulphuric acid solutions. *J. Electroanal. Chem. Interfacial Electrochem.* **205**, 267–277 (1986).
33. Clavilier, J., El Achi, K. & Rodes, A. In situ probing of step and terrace sites on Pt(S)-[$n(111) \times (111)$] electrodes. *Chem. Phys.* **141**, 1–14 (1990).
34. Michaelis, R. & Kolb, D. M. Stability and electrochemical properties of reconstructed Pt(110). *J. Electroanal. Chem.* **328**, 341–348 (1992).
35. Wonders, A. H., Housmans, T. H. M., Rosca, V. & Koper, M. T. M. On-line mass spectrometry system for measurements at single-crystal electrodes in hanging meniscus configuration. *J. Appl. Electrochem.* **36**, 1215–1221 (2006).
36. Grimaud, A. et al. Activating lattice oxygen redox reactions in metal oxides to catalyse oxygen evolution. *Nat. Chem.* **9**, 457 (2017).
37. Iwasita, T., Nart, F. C. & Vielstich, W. An FTIR study of the catalytic activity of a 85:15 Pt:Ru alloy for methanol oxidation. *Ber. Bunsenges. Phys. Chem.* **94**, 1030–1034 (1990).
38. Kresse, G. & Furthmüller, J. Efficient iterative schemes for ab initio total-energy calculations using a plane-wave basis set. *Phys. Rev. B* **54**, 11169–11186 (1996).
39. Perdew, J. P., Burke, K. & Ernzerhof, M. Generalized gradient approximation made simple. *Phys. Rev. Lett.* **77**, 3865–3868 (1996).
40. Kresse, G. & Joubert, D. From ultrasoft pseudopotentials to the projector augmented-wave method. *Phys. Rev. B* **59**, 1758–1775 (1999).
41. Monkhorst, H. J. & Pack, J. D. Special points for Brillouin-zone integrations. *Phys. Rev. B* **13**, 5188–5192 (1976).
42. Nørskov, J. K. et al. Origin of the overpotential for oxygen reduction at a fuel-cell cathode. *J. Phys. Chem. B* **108**, 17886–17892 (2004).
43. Calle-Vallejo, F. & Koper, M. T. M. Theoretical considerations on the electroreduction of CO to C₂ species on Cu(100) electrodes. *Angew. Chem. Int. Ed.* **52**, 7282–7285 (2013).
44. He, Z.-D., Hanselman, S., Chen, Y.-X., Koper, M. T. M. & Calle-Vallejo, F. Importance of solvation for the accurate prediction of oxygen reduction activities of Pt-based electrocatalysts. *J. Phys. Chem. Lett.* **8**, 2243–2246 (2017).
45. Calle-Vallejo, F., Martínez, J. I., García-Lastra, J. M., Sautet, P. & Loffreda, D. Fast prediction of adsorption properties for platinum nanocatalysts with generalized coordination numbers. *Angew. Chem. Int. Ed.* **53**, 8316–8319 (2014).
46. Calle-Vallejo, F., Sautet, P. & Loffreda, D. Understanding adsorption-induced effects on platinum nanoparticles: an energy-decomposition analysis. *J. Phys. Chem. Lett.* **5**, 3120–3124 (2014).
47. Calle-Vallejo, F. et al. Finding optimal surface sites on heterogeneous catalysts by counting nearest neighbors. *Science* **350**, 185–189 (2015).
48. Calle-Vallejo, F., Pohl, M. D. & Bandarenka, A. S. Quantitative coordination-activity relations for the design of enhanced Pt catalysts for CO electro-oxidation. *ACS Catal.* **7**, 4355–4359 (2017).

Acknowledgements

This research received funding from the Netherlands Organization for Scientific Research (NWO) in the framework of the fund New Chemical Innovations (project 731.015.204 ELECTROGAS) with financial support from Akzo Nobel Chemicals, Shell Global Solutions, Magneto Special Anodes (Evoqua Water Technologies) and Elson Technologies. F.C.-V. thanks the Spanish MEC for a Ramón y Cajal research contract (RYC-2015-18996) and acknowledges financial support from the Units of Excellence Maria de Maeztu programme through grant MDM-2017-0767. The use of supercomputing facilities at SURFsara was sponsored by NWO Physical Sciences, with financial support by NWO.

Author contributions

C.J.B. co-conducted the FTIR experiments and conducted the remaining experimental work (that is, CV, OLEMS and surface enhanced Raman spectroscopy studies), co-conceived the concept of the presented work and co-wrote the manuscript. F.C.V. conducted the theoretical modelling, co-conceived the concept of the presented work and co-wrote the manuscript. M.C.F. co-conducted the FTIR experiments. M.T.M.K. co-conceived the concept of the presented work and co-wrote the manuscript.

Competing interests

The authors declare no competing interests.

Additional information

Supplementary information is available for this paper at <https://doi.org/10.1038/s41929-019-0229-3>.

Reprints and permissions information is available at www.nature.com/reprints.

Correspondence and requests for materials should be addressed to M.T.M.K.

Publisher's note: Springer Nature remains neutral with regard to jurisdictional claims in published maps and institutional affiliations.

© The Author(s), under exclusive licence to Springer Nature Limited 2019